

Optical near-field response of semiconductor quantum dots

B. Hanewinkel, A. Knorr, P. Thomas, and S.W. Koch

Department of Physics and Material Sciences Center, Philipps-Universität, Renthof 5, D-35032 Marburg, Germany

(Received 3 December 1996)

The near-field response of optically excited semiconductor quantum dots is theoretically investigated for the collection and illumination mode of a scanning near-field optical microscope. The study includes resolution, spectral line shape, and field distributions of single and interacting dots. It is shown that in contrast to near-field excitation of molecules with large dipole moments, the line shape and position of typical semiconductor quantum dots can be determined without a disturbance if realistic values for the intrinsic linewidth are assumed. The comparison of regular and irregular quantum-dot distributions yields characteristic signatures for disordered arrays, necessary to understand the optical response of realistic semiconductor quantum dot samples. [S0163-1829(97)04620-1]

I. INTRODUCTION

Experimental studies of semiconductor quantum-dot systems using conventional optical techniques, such as pump-probe spectroscopy, nonlinear wave mixing, etc., yield in most cases information only of the spatially averaged system properties. Since real samples usually contain distributions of dot sizes, shapes, or composition,^{1,2} the signals are often dominated by inhomogeneous broadening, masking many of the signatures of the individual quantum dots. In addition to the experimental preparation of ultimate samples, which contain no or drastically reduced distributions, experimental information on the optical properties of individual dots can be obtained only by using optical techniques with subwavelength spatial resolution.^{3,4}

A very promising tool for high spatial resolution optical measurements are the recently developed scanning near-field optical microscopes (SNOM's).⁵ Here, modifications of electromagnetic radiation are detected which are caused by the interaction of the microscope tip with an object smaller than the wavelength of light. Hence SNOM's seem to be ideally suited to investigate the properties of individual quantum dots within a dot ensemble realized in a realistic structure. In order to investigate the potential and limitations of the SNOM technique we perform model calculations for idealized near-field geometries. For such a study it is especially important to analyze the characteristic signatures of the scanning near-field source or detector, i.e., the tip of a SNOM, and to extract those signatures which are caused by the interaction with the quantum dot. Since tip and dot are of comparable spatial dimension, one has to investigate the strongly coupled configuration of quantum dots and tip. In the vicinity of the tip, electromagnetic fields are strongly altered by the object (quantum dot) and thus, scanning the aperture over a sample, subwavelength resolution by means of an optical experiment is achieved. Often, in the experimental setup the aperture is a fiber tip scanning over the sample. In principle, the fiber tip can be used either for collecting the radiation of the sample or for exciting the sample. The use of a tip smaller than or comparable to the wavelength of light as a optical source has several features different from the illumination by a plane wave or lense focused laser source. First,

there is the strong localization of radiation below the diffraction limit, thus allowing an enhanced optical resolution. Second, the near-field creating source is close to the sample, which implies the existence of longitudinal field components interacting with the sample. Third, analytical models, like the Bethe-Bouwkamp solutions^{6,7} for the electromagnetic fields behind a small circular aperture, often used as a model for a fiber tip, suggest a strong enhancement of magnetic field components in comparison with the electric fields. This enhancement of the magnetic fields makes the near-field method not only very efficient to study magnetic materials but it may be possible that for strong enhancement the established multipole ordering of the Hamiltonian could break down, because the reduced strength of the magnetic material moments in comparison with the electric dipole moments can be compensated by the magnetic field enhancement. This behavior, however, is only expected for very small apertures whose diameter is much smaller than the wavelength of incident light. As shown below, for tips used in current experiments, electric and magnetic field show the same order of magnitude, thus favoring electric field effects.

First calculations and their experimental verification of matter-field interaction have been presented for field distributions,⁸ their polarization dependence,⁹ and line shapes of single molecules exposed to fiber tips.^{10,11} Investigations of the molecule-tip interaction show that the linewidth of a molecule is strongly dependent on the respective position of tip and molecule, thus allowing for the conclusion that measured lifetimes are changed in comparison to the intrinsic lifetimes, which in turn are given by spontaneous emission in the presence of the vacuum field and other reservoir processes. This behavior results from the strong coupling regime of molecule and tip, due to a large dipole moment and very long intrinsic lifetimes of the molecule transitions. Besides these studies of molecular systems recent experiments are also applied to manmade solid state devices, such as quantum dots and wells.¹²

In this paper, we go beyond preliminary calculations theoretically investigating a SNOM experiment in the vicinity of a quantum dot array. As a detector/source with a subwavelength aperture we assume a metal coated fiber tip, which may collect the scattered radiation after excitation of the dot

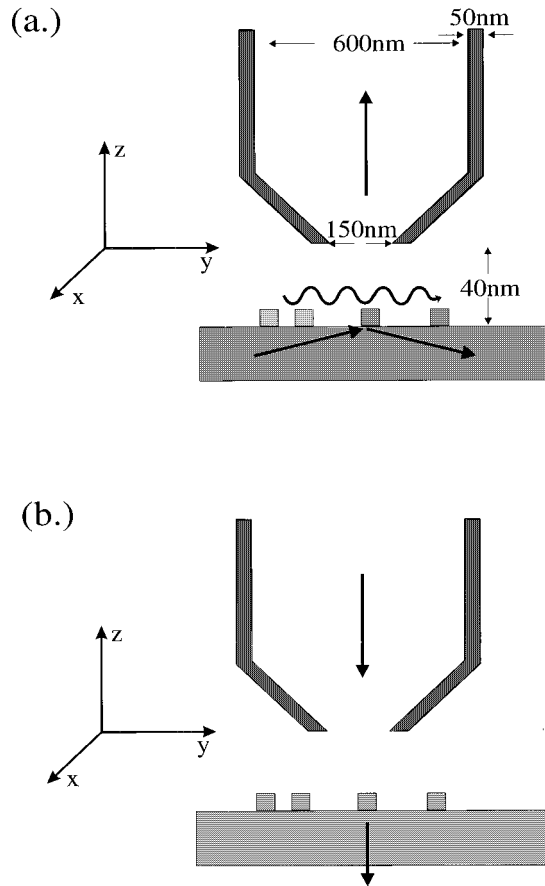


FIG. 1. Sketch of SNOM experiment, working in (a) collection and (b) illumination mode.

array with a plane wave, thus working in the collection mode. Alternatively, this arrangement allows the excitation of the dots through the tip within the illumination mode.

The paper is organized as follows. The treatment of the electromagnetic field and matter is briefly reviewed and a description of the considered geometry and calculated observables is given in the following Sec. II. The model for the interaction of the electromagnetic field of the tip and the quantum-dot system is outlined in Sec. III. In Sec. IV spatially resolved optical properties of single dots and dot arrays are discussed. Our results are summarized in Sec. V. In two appendixes we summarize the main steps of the Green function method to solve the electromagnetic wave equation for the tip (Appendix A) and we discuss the material equations used to describe the quantum-dot system (Appendix B).

II. GEOMETRY AND OBSERVABLE QUANTITIES

As a realistic model system for near-field optical microscopy we study an array of resonantly excited semiconductor quantum dots located on a dielectric, nonabsorbing substrate with a fixed and frequency independent refractive index. Two basic modes for the tip-dot interaction will be analyzed: (i) collection mode and (ii) illumination mode. These configurations are schematically shown in Figs. 1(a) and 1(b), respectively.

(i) *Collection mode.* A plane excitation wave under an angle of total reflection is incident from the bottom of the

substrate thus inducing evanescent surface waves traveling on the surface of the substrate¹⁰ and interacting with the quantum-dot ensemble. On top of this geometry, a SNOM detector working in collection mode is applied. The field emitted by the quantum dots is collected by the tip. At the end of the tip (L_0) a photodetector measures the energy flux density (poynting vector) of the radiation integrated over the whole area of the tip $w(L_0)$:

$$w(L_0) = \frac{c}{4\pi} \int \int dx dy \operatorname{Re}(\mathbf{E} \times \mathbf{H}^*)_z. \quad (1)$$

In general, these calculations have to be done until the tip length and the thickness of the fiber allows for a propagating mode. However, in the numerical scheme we use (see Appendix A) this requires immense calculational effort, thus we restrict the calculations to that length of the fiber tip where the flux through different planes of the fiber remains qualitatively unchanged; besides a gradual decrease due to a finite penetration depth. The analysis shows that these conditions are satisfied at a length where the tip diameter has increased to a value exceeding the wavelength λ . This approach is consistent with the cut-off wavelength of the fiber and indicates that the calculated signal is propagated through the fiber, finally arriving at the detector, see Ref. 13.

(ii) *Illumination mode.* As a second example, the illumination mode is investigated. Here, the tip is used as a near-field source and spatial resolution is obtained by scanning this source over the sample and detecting the resulting changes in the far field. To generate the near field, it is assumed that a beam with Gaussian profile is propagated through the fiber until it reaches the tip and its transmission through the tip hole yields to an optical near field.

As observable quantity the intensity of the electromagnetic field \mathbf{E} at a position \mathbf{r}_0 in the far field is detected by a pointlike photodetector. To remove the background, its relative change

$$S(\mathbf{r}_0) = \frac{|\mathbf{E}|^2 - |\mathbf{E}_0|^2}{|\mathbf{E}_0|^2} \quad (2)$$

due to the presence of the sample is calculated. Here, \mathbf{E}_0 denotes the field without the sample, \mathbf{E} is the field which includes the full geometry. Our numerical calculations indicate that at a distance of $3 \times \lambda$ the obtained results are already a good approximation of the far field. In this geometry, the absorption line shape, defined by the induced polarization $\mathbf{P}(\omega)$ is investigated as a function of tip position and coupling strength between tip and dot.

Now, after having briefly described the basic two interaction modes, the corresponding fields must be calculated to obtain the observable quantities. The used equations and their derivation are outlined in the next section.

III. FIELD-QUANTUM-DOT INTERACTION

In this section we briefly sketch the method to solve the vector Maxwell's equations for the full electric field in the linear domain.⁹ We consider the wave equation of the total electric field including transverse and longitudinal components:

$$\nabla^2 \mathbf{E} - \nabla \nabla \cdot \mathbf{E} - \frac{1}{c^2} \frac{\partial^2}{\partial t^2} \mathbf{E} = \frac{4\pi}{c_0^2} \frac{\partial^2}{\partial t^2} \mathbf{P}. \quad (3)$$

In the strict regime of linear optics, using a linear susceptibility χ , the polarization can be written in the Fourier domain as

$$\mathbf{P}(\mathbf{r}, \omega) = \chi(\mathbf{r}, \omega) \mathbf{E}(\mathbf{r}, \omega). \quad (4)$$

Here, we have assumed that the medium has no optical anisotropy and a local response. The assumption of a local response restricts the application to localized carriers, a situation well realized in a semiconductor quantum dot where the spatial confinement is complete in all spatial directions.¹ However, in principle this restriction is not necessary, and can be relaxed, e.g., for the study of semiconductor wires, wells, and bulk materials. The total polarization is subdivided into nonresonant contributions (background or reference medium subscript r) and the resonant or nonresonant perturbation (subscript p). Thus we can write the susceptibility as

$$\chi = (\chi_r + \chi_p). \quad (5)$$

Using the definition of the dielectric function ε and combining the susceptibility with the wave equation, we arrive at

$$\nabla^2 \mathbf{E} - \nabla \nabla \cdot \mathbf{E} + \frac{\omega^2}{c_0^2} [\varepsilon_r(\omega, r) + \varepsilon_p(\omega, r)] \mathbf{E} = 0. \quad (6)$$

Similarly, for the magnetic field we have the following wave equation:

$$\nabla^2 \mathbf{B} + \frac{\omega^2}{c_0^2} \mathbf{B} = 4\pi i \frac{\omega}{c_0} \nabla \times \mathbf{P}. \quad (7)$$

Having solved Eq. (6) the polarization is given by Eq. (4) and thus the magnetic field \mathbf{B} can be calculated by Eq. (7). The solution of this system of equations can be obtained numerically by using an efficient calculation scheme proposed in Ref. 9. The scheme is based on a Green function approach, which consists of a self consistent set of Lippmann-Schwinger and Dyson-equations for the corresponding Green functions of the perturbed and unperturbed system, respectively. This method is briefly reviewed in Appendix A.

We apply this method to study an array of quantum dots interacting with an external electromagnetic field which fulfills the appropriate boundary conditions at the tip and at the quantum dots. To calculate the fields, the susceptibility of the array must be determined. The different quantum dots are well localized in space, their extension is assumed to be much smaller than the variation length of the electromagnetic field. Thus, they are treated as point like particles with respect to the spatial changes of the light field. Under rather general assumptions their susceptibility can be cast into the following form (see, e.g., Ref. 1):

$$\chi(\mathbf{r}, \omega) = \frac{i}{\Omega_0} \sum_{i,j,\kappa} \frac{|d_{ij}|^2 f_{ij}}{\Gamma_{ij} + i(E_i - E_j - \omega)} \delta(\mathbf{r} - \mathbf{r}_\kappa). \quad (8)$$

Here i, j , denote the different quantum states in the quantum dot, placed at \mathbf{r}_κ , d_{ij} are the matrix elements of the dipole

operator, and Ω_0 is the volume of the elementary cell. Γ_{ij} are the intrinsic polarization decay rates and will be chosen to be constant ($\Gamma_{ij} = \Gamma_0$). f_{ij} denotes a static band filling factor, which is one for small excitation and is negative for inversion. For simplicity we discuss the case of resonant or nearly resonant excitation of one transition ($1 \rightarrow 2$), thus neglecting nonresonant terms. For a detailed discussion of the material equations and their validity in the case of near-field interaction see Appendix B. Using the susceptibility, Eq. (8), in the wave equation (6) the problem of near-field - dot interaction is formulated self-consistently.

IV. APPLICATIONS

In this section, equations for the electromagnetic field under the influence of the coupled material system of fiber tip and semiconductor quantum dots are solved for several scenarios. First, we characterize the action of the tip on the electromagnetic field and discuss how a plane wave/Gaussian pulse used as excitation field develops into a near-field distribution for both, illumination and collection mode. Second, the interaction of the field with single quantum dots and with various dot arrays is discussed.

A. Characterization of the fiber tip

In the following calculations, the tip is modeled as a metal coated fiber having a quadratic shaped hole, oriented parallel to the axes of the coordinate system. Its aperture is 150 nm in each direction. The opening angle is 90° . The metallic film is 50 nm thick, for the calculation the interior dielectric is chosen to be vacuum, assuming that the main influence on the field is given by the metallic coating. In the following we assume that the field propagates through the fiber from the positive z direction to the negative z direction (illumination mode) or in the opposite direction reaching the detector at the end of the fiber tip (compare Fig. 1). If not mentioned otherwise, the polarization of the incoming wave is always chosen to be in the x direction.

1. Illumination mode

In this mode, the tip is excited by a Gaussian beam propagating into the tip [compare Fig. 1(b)]. The dielectric surface depicted in this figure is not taken into account in the following calculations.

In Figs. 2 and 3 we plot the spatial distribution of the electric and the magnetic field, respectively, after transmission through the fiber tip. Figure 2(a) shows the spatial distribution of the field in the propagation direction at different (x, y) . It can be recognized that the incoming field and the field reflected from the front of the tip interfere within the fiber $z > 0$ for $(x=0, y=0)$. The evanescent field is seen to decay rapidly after its transmission through the hole at $z < 0$. In addition to this we also plot in Fig. 2(a) the field close to the walls of the tip, $x=0.1 \mu\text{m}$ or $y=0.1 \mu\text{m}$, respectively. We clearly recognize a dramatic field enhancement near the walls. Figure 2(b) and Fig. 2(c) shows the spatial field distribution in x, y direction for different distances outside the tip. One clearly recognizes the difference of the field structure in x and y direction. Whereas for the y direction, i.e., perpendicular to the polarization of the in-

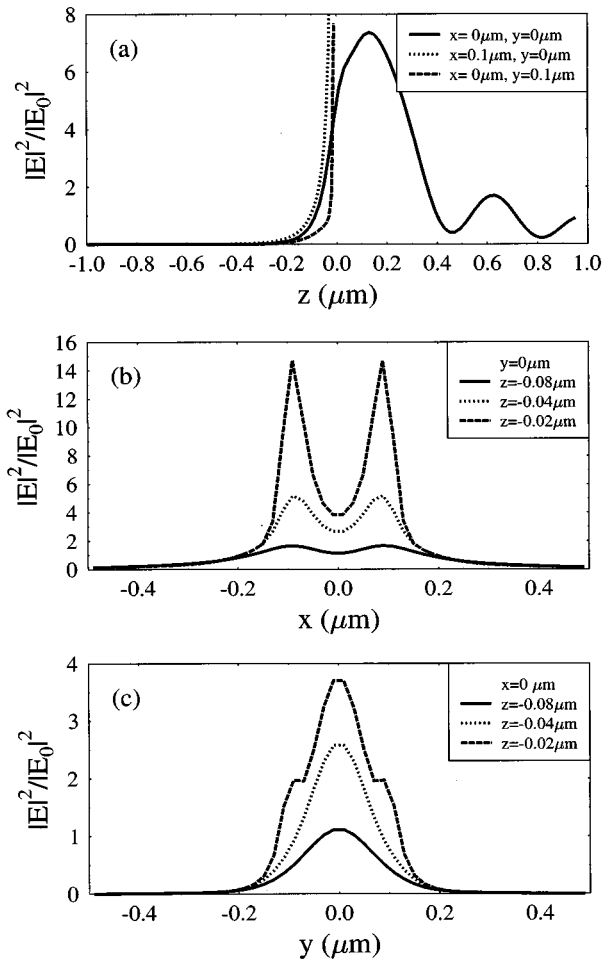


FIG. 2. Electric field intensity under a tip in illumination mode (a) in propagation direction, (b) in polarization direction, and (c) perpendicular to both directions. The incoming field is modeled by a Gaussian beam with beam waist at $x=y=0\mu\text{m}$. The intensity is normalized to the intensity of the incoming field in this point. The tip has an aluminium coating of 50 nm thickness, its dielectric constant is $-26.3+5.2i$. The aperture has a diameter of 150 nm. The tip ranges vertically from $z=0$ to $z=1\mu\text{m}$, horizontally it is centered in $x=y=0\mu\text{m}$. The wavelength of the incoming (in a $-z$ direction) light is 628 nm.

coming field, a localized distribution is obtained, a double peaked structure occurs for the x direction in which the incoming field is polarized. This is similar to the field distribution in a circular aperture, where the electric field diverges in the polarization direction at the rim.⁷ The z dependence shows the length within which the evanescent field spatially decays, indicating a decay length of $k^{-1}=\lambda/2\pi$. The height of the double peak observed in x direction gradually decreases with an increasing distance from the tip.

A similar scenario as discussed for the electric field can be found for the magnetic field in Fig. 3. Similar to the field distribution in an aperture of an ideal conducting plane the magnetic field perpendicular to the polarization direction is enhanced. The ratio B/E depends on the position relative to the tip. It is mostly smaller than one and does not exceed a value of three in the observed region. This indicates that for the tip geometry studied here the material interaction with the magnetic field can be neglected, similar as in the far-field

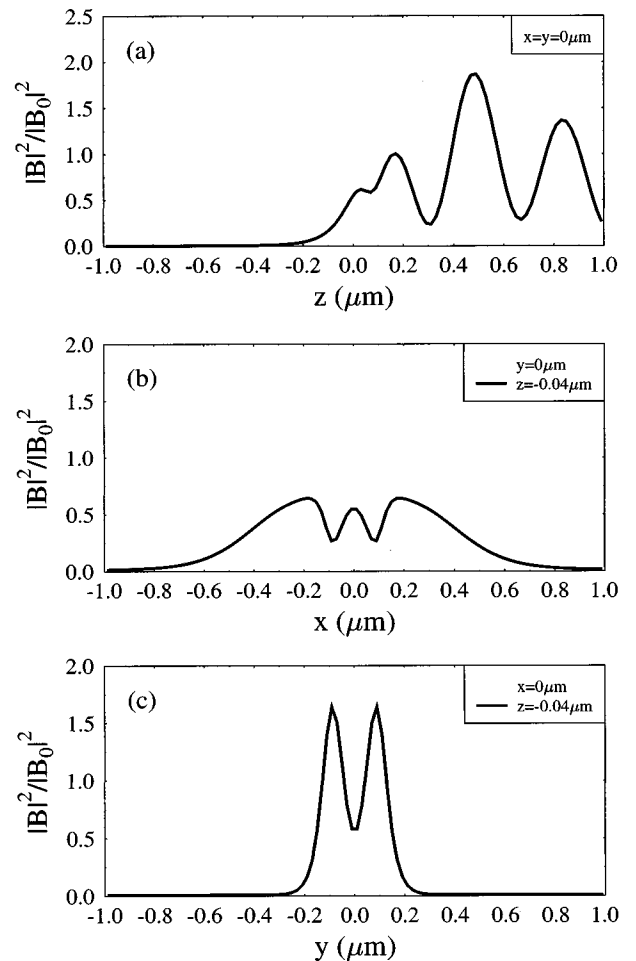


FIG. 3. Magnetic field distribution under a tip in illumination mode, same setting as in Fig. 2.

geometry (see Appendix B for a detailed discussion).

A characteristic length scale for the variation of both electric and magnetic field is 40 nm. This means that a multipole expansion as performed in the Hamiltonian (see Appendix B) is only useful if the sample is smaller than 40 nm, because only in this case higher order multipole terms can be neglected. However, for the case of quantum dots with a typical diameter of an excitonic Bohr radius (10 nm) studied here, the neglect of all but the dipole contributions is an excellent approximation.

2. Collection mode

To characterize the collection mode, we first calculate the field distribution only in the presence of the dielectric substrate with no quantum dots on it. Figures 4(a) and 4(b) show the resulting electric field intensity under the tip. We assume plane wave excitation with parallel [Fig. 4(a)] or perpendicular [Fig. 4(b)] polarization with respect to the plane of incidence. The distance of tip to surface is 40 nm, the field is calculated 20 nm above the surface.

The comparison of Fig. 4(a) and Fig. 4(b) clearly demonstrates that the field distribution corresponding to parallel or perpendicular polarization differs drastically in magnitude. To understand these differences we can think of the tip in the collection mode as dipole induced by the wave traveling on

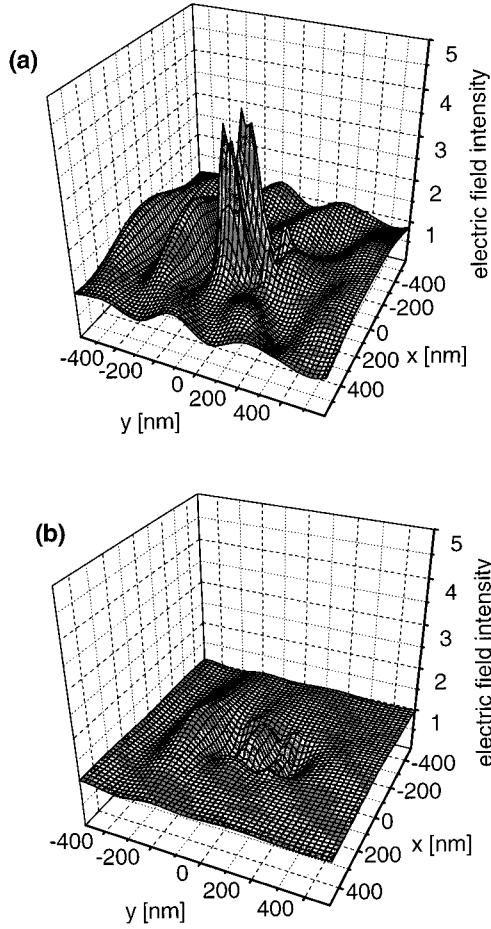


FIG. 4. Electric field intensity under a tip in collection mode. Height of tip above the surface: 40 nm, plane of observation 20 nm. The tip is the same as in Fig. 2. The refractive index of the surface is $n = 1.5$. The field is normalized to the intensity of the evanescent surface wave traveling without the tip, (a) polarization of incoming wave in plane of incidence (y, z plane), (b) polarization of incoming wave perpendicular to plane of incidence (x direction).

the substrate. This induced dipole is oriented corresponding to the polarization of the substrate-guided wave which, in turn, is determined by the incident waves. The direction of the induced dipole is perpendicular (parallel) to the surface for incident waves polarized parallel (perpendicular) to the plane of incidence. Due to the boundary conditions, the total field can be approximated by the dipole field plus a mirror dipole field on the other side of the surface, which is oriented parallel in the case of a dipole perpendicular to the surface and antiparallel otherwise. In the first case direct and mirror field add constructively, whereas they add destructively in the second case. In the following we concentrate on parallel incidence, depicted in Fig. 4(a) because a larger field enhancement is expected to improve the signal from a source under the tip. In this case it can be recognized that the electric field is strongly enhanced under the metallic edges of the tip. In addition, strong interference effects occur as indicated by the oscillating electric field distribution. The evanescent surface wave is partly reflected by the tip. Thus, in front of the fiber standing waves occur, whereas behind the fiber tip a weak, spatially decaying field is observed. This behavior is similar to the transmission of a traveling wave through a

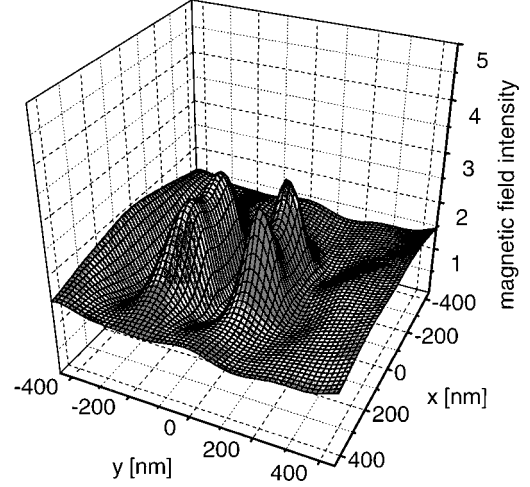


FIG. 5. Magnetic field intensity under the tip in the collection mode, parameters as in Fig. 4(a).

barrier. Similar calculations for a dielectric tetrahedral tip in the same experimental setup¹⁰ yield a strongly peaked field distribution, in contrast to our case where we get a fine structure resembling the shape of the tip.

For comparison with the electric field distribution, the magnetic field distribution has been calculated in Fig. 5. While the electric field is peaked under the edges parallel to the propagation direction of the surface wave (y direction) the magnetic field distribution peaks under the edges of the tip, perpendicular to the propagation direction. Thus the ratio of electric to magnetic field has a strong spatial dependence. The maxima are approximately equal. For even smaller tips, where the magnetic field is further enhanced, there may exist spatial areas, where the magnetic and the electric interaction can be comparable.

B. Quantum-dot response

To study the interaction with quantum dots we first assume the case of a single dot before quantum-dot arrays are investigated. As before, we analyze the illumination and collection mode separately. For simplicity, we restrict the study of a dot array to a linear chain of dots extended in x direction. The susceptibility of the dots is chosen corresponding to Eq. (8). Here, we use the following parameters: $\chi_0 = 4\pi\chi(\omega_0)/i$ denotes the susceptibility under resonant excitation. The values ($\chi_0 = 0.1, 1, 10$) correspond to a dipole strength $d = 3 \text{ eÅ}$, whereas the intrinsic dephasing rate Γ_0 is varied from $\Gamma = 10^{-5}$, $\Gamma = 10^{-6}$ to $\Gamma = 10^{-7}$ (in units of ω_0) to study the weak and strong coupling regimes between the dot and near field. Note that a susceptibility smaller than zero ($\chi_0 = -1$) results in inverted quantum-dot levels [negative f in Eq. (8)], thus characterizing optical gain. To obtain realistic values for quantum-dot arrays which are under experimental study,¹² the parameters have to be chosen in the range described above.

1. Illumination mode

(i) *Single dots.* Figure 6(a) shows the computed far-field signal S at $\mathbf{R}_0 = (0, 0, -2) \mu\text{m}$, Eq. (2), as a function of the scanning distance x of the tip with respect to a single dot at

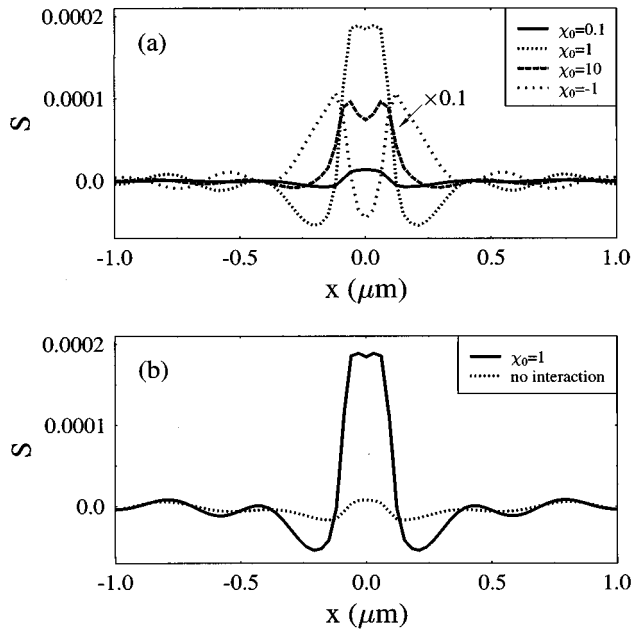


FIG. 6. (a) Signal of a dot in the illumination mode for various χ_0 , the dot is placed at $x=0$ and 40 nm under the tip. The scanning direction is parallel to the polarization of the incoming light (x direction). (b) Signal of a dot in the illumination mode for $\chi_0=1$, with and without the neglect of the near-field interaction.

the position $x=0$. The different curves represent a set of different susceptibilities of the dot $\chi_0=0.1, 1, 10, -1$. It can be recognized that an interference pattern is formed due to the superposition of the field of the tip and the induced dipole of the quantum dot. The main signal contribution is peaked at the dot position because here the induced dipole field is strongest. However, a weak interference pattern resulting from the interference between the induced polarization and the tip field extends up to several tip diameters away from the dot.

The signal rises with increasing quantum dot susceptibility and changes its behavior qualitatively. For small susceptibilities the observed signal has only weak modulations, whereas for large susceptibilities a double peaked structure develops. This double peak structure follows the positions of the tip walls with respect to the quantum dot and is a direct consequence to the electric field enhancement below the walls of the tip in the strong coupling regime [compare Fig. 2(b)].

For the dot having optical gain ($\chi_0 = -1$) we see a more or less inverted signal with respect to that of an absorbing dot with the same absolute value of χ_0 . Thus, we conclude that within a near-field study the optical absorption and gain of single dots can be distinguished as long as a single dot is covered by the area of the tip focus. This situation is of particular interest for quantum-dot gain media where typically only a fraction of the dots experiences gain after the arrival of an optical pump or a pump current due to the inhomogeneous distribution in the dot array.¹

A typical difference between near-field and far-field optics is that the sources of the incident radiation cannot be neglected in a near-field situation. To study the influence of the sources (in our case the fiber tip), we compare the full

solution with the situation where the interaction of dot and tip material is neglected [Fig. 6(b)]. We see that without near-field interaction the signal is much less pronounced, and its maximum is about one order of magnitude smaller. The ratio of the maximum to the surrounding wiggles is decreased, so that a detection of the dot is more difficult. Only for increasing distance of dot and tip the interaction becomes weaker and the difference between both signals gradually decreases. This shows that the sources of the near field have a strong effect on the signal and cannot be neglected.

We also discuss the line shape of the polarization at the position of the dot. The line shape and position contain information on the polarization decay and a possible line shift in the presence of a near-field tip. The line shape L of the dot is defined as the frequency dependent polarization $L=|P(\omega)|$ at the position of the dot for a pulse $E_0 \sim \delta(t)$ containing all frequencies ω with a unit amplitude. Note that for a dot in a homogeneous surrounding (far field excitation) the line shape is proportional to (see Ref. 13)

$$|P(\omega)| = \frac{3}{4\pi} \left(\frac{\epsilon - 1}{\epsilon + 2} \right) = \chi \left(\omega - \frac{\chi_0}{3} \Gamma_0 \right). \quad (9)$$

Hence the line shape is determined by the susceptibility, with a shifted resonance frequency. This line shape shows the width determined by the intrinsic decay $\Gamma_0 \equiv \Gamma_{12}$ of the transition and the polarization would decay within Γ_0^{-1} in a pulsed excitation.

Because we are interested in the modification of the decay time and the line shape due to the near field we study the situation where the unit field E_0 has to travel through the tip before arriving at the position of the dot. Figure 7 shows the line shape for different intrinsic lifetimes, depending on the distance from the center of the tip. The frequency shift due to Eq. (9) has been compensated for.

From Fig. 7 it can be recognized that the line shape in presence of the tip depends strongly on the intrinsic life time $\sim 1/\Gamma_0$. Even for long lifetimes, $\Gamma_0 = 10^{-7}$, $\chi_0 = 10$ the observed near-field line shape resembles more or less the far-field line shape, thus indicating the possibility for an error-free measurement of the intrinsic line shape. However, if we increase the lifetime even further a line broadening, and for very high couplings, line shape modifications and even a splitting of the lines is observed. The linewidth broadening has been observed and theoretically calculated for molecules on a substrate.¹⁰ However, to our knowledge, the linewidth splitting for very high couplings has not been discussed so far.

(ii) *Linear quantum dot arrays.* In contrast to atomic physics where the study of single molecules/atoms is desirable, in solid state device optics one is often interested in having a high dot density to optimize the emission and non-linear properties of quantum-dot samples. Here, due to the strong inhomogeneous broadening, which spatially modulates the optical properties of the quantum dot samples, a near-field study with high spatial resolution is desirable. The resolution of single dot properties such as optical gain or absorption using the near-field method will strongly depend on the density of the dots and their interaction strength. A reasonable measure of the dot density N_0 is in dots per average spot size of the near-field tip. A typical sample is, e.g.,

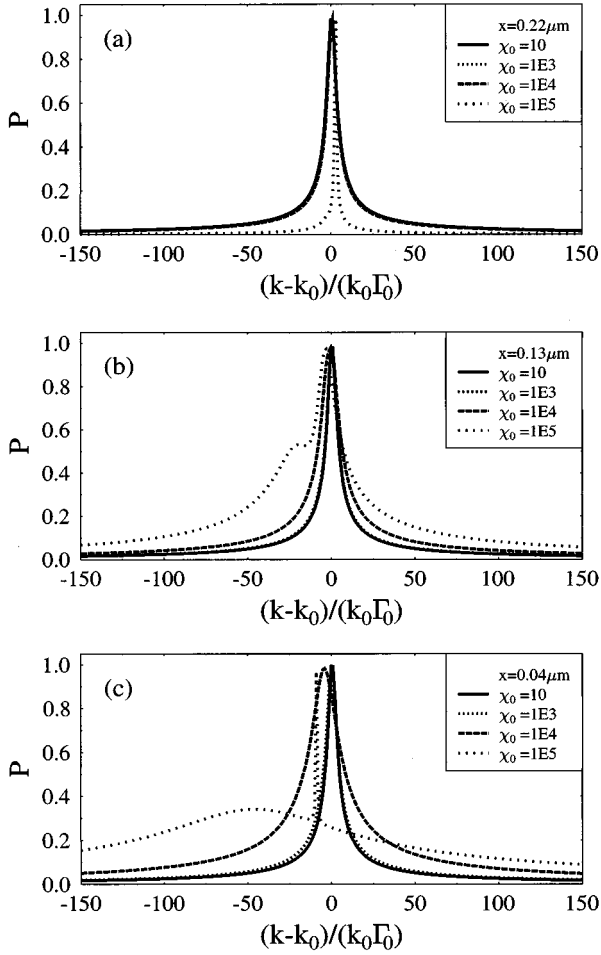


FIG. 7. Line shape study. Each curve represents the line shape of a dot placed in distance x (in polarization direction) from the center of the tip, the line shape is given in units of the intrinsic linewidth and the curves are normalized to a maximum of one.

described in Ref. 14 where the dot density is approximately $N_0=0.5$. For this situation it should be possible to resolve single dots as long as they are more or less uniformly distributed. Figure 8(a) shows the computed far-field response $S(x_0)$ for a scan of a linear quantum-dot array equally distributed in x direction at a density of $N_0 \approx 0.3$ ($\chi_0=1$, $\Gamma_0=10^{-6}$). At this density the individual quantum dots are easily resolved and even a line shape analysis yields the same answer as that of a single dot (not shown). The modification of the signal due to the presence of several dots are negligible at the positions of the dot. However, in the regions between the dots, field interference strongly changes the signal distribution, because here the induced fields of neighboring dots are comparable. However, the signal to background contrast is even increased due to the destructive interference in the presence of a small dot density.

In contrast to this idealized configuration, in real samples local clusters of dots may complicate the analysis even if the average dot density is low. Figure 8(b) shows a scan for five dots at a distance of 100 nm which is comparable to the density $N_0=2.5$. The observed signal indicates that the dots react as a cluster of dipoles within the tip spot. A strong interference of the individual dot signals modulate the total

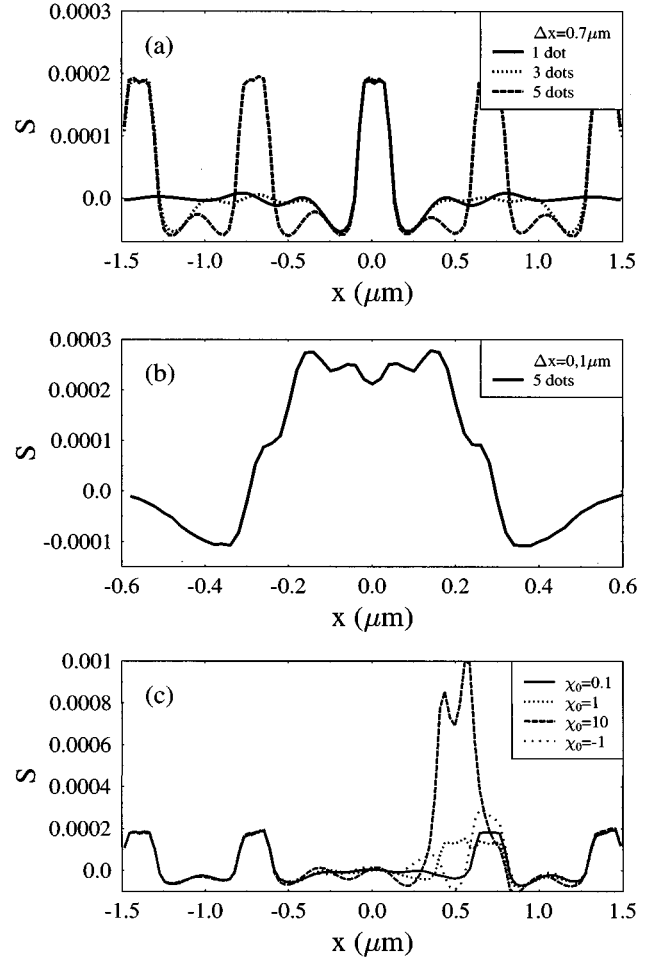


FIG. 8. Far-field signal S for different arrays of dots. (a) Regular array of 1, 3, 5 dots with a distance $\Delta x=0.7 \mu\text{m}$. The dots are at $x=0 \mu\text{m}$; at $x=-1.4 \mu\text{m}$, $0 \mu\text{m}$, $1.4 \mu\text{m}$ and at $x=-1.4 \mu\text{m}$, $-0.7 \mu\text{m}$, $0 \mu\text{m}$, $0.7 \mu\text{m}$, $1.4 \mu\text{m}$. (b) Five dots with distance $\Delta x=100 \text{ nm}$, centered in $x=0$. (c) Disordered array, one dot is assumed to be displaced. The different curves correspond to different susceptibilities of the displaced dot.

response. The spatial width of the observed signal is 2–3 times larger than the tip width. From such an experimental measurement it could only be concluded that several dots are distributed within the focus.

In general, the analysis of a quantum dot ensemble is difficult not only for large dot densities but also due to the occurring inhomogeneous size distribution which modulates the transition energies and thus the susceptibilities. To model this behavior we have studied a regular sample of dots where the properties of one irregularly positioned dot is different in comparison to the surrounding dots. Figure 8(c) shows a plot where the surrounding dots have the same parameters as in Fig. 8(a), however, the dot that was originally positioned at $x_0=0$ is now shifted to the position $x_0=500 \text{ nm}$. In addition the shifted dot has a different susceptibility $\chi=0.1, 1, 10, -1$. If the shifted dot has a much smaller susceptibility ($\chi_0=1$) than the surrounding dots it can hardly be detected. If the two closely spaced dots have the same susceptibility ($\chi_0=1$) they show again the cluster effect and a broader spatial width than the tip size, whereas for different

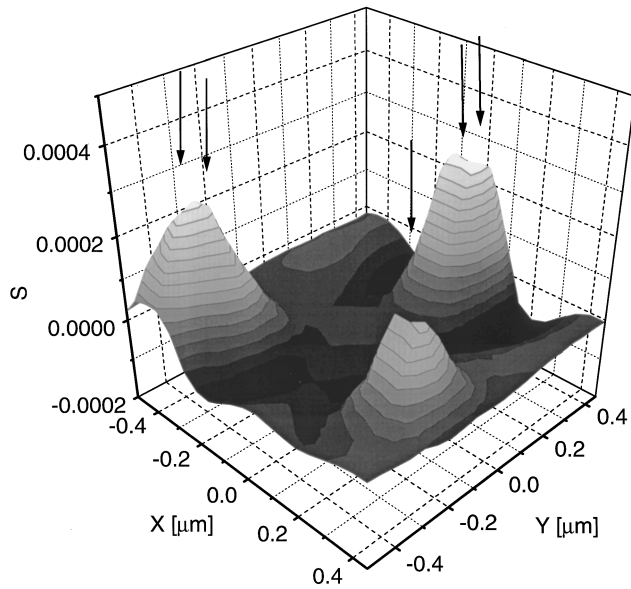


FIG. 9. Signal of five dots in the collection mode, the dots are placed in $(-0.4, -0.4)\mu\text{m}$, $(-0.3, -0.3)\mu\text{m}$, $(0, 0.3)\mu\text{m}$, $(0, 0.2)\mu\text{m}$, and $(0.3, -0.2)\mu\text{m}$.

susceptibilities ($\chi_0=10$) the dot in the weak coupling regime is strongly suppressed in comparison to the dot with the high susceptibility. In the case that the shifted dot has gain, due to interference effects, the signal of the other dot is enhanced. However, the field distribution of the individual dots, surrounding the distortion is not strongly altered.

Figure 9 presents the calculated results for a two dimensional scan over five dots at the positions $(-0.4, -0.4)\mu\text{m}$, $(-0.3, -0.3)\mu\text{m}$, $(0, 0.3)\mu\text{m}$, $(0, 0.4)\mu\text{m}$, and $(0.3, 0.2)\mu\text{m}$ with $\chi_0=1$. We see that the two pairs of closely spaced dots cannot be resolved, they appear as one dot with a slightly higher susceptibility. In principle, using our calculations and making assumptions on the linewidth Γ_0 , experimentally observed mappings of quantum dot arrays could be reconstructed.

2. Collection mode

(i) *Single dots.* Figure 10 presents the calculated energy flux Eq. (1) for different relative positions of the tip and sample in the x - y plane having one quantum dot positioned at the origin of the x - y plane. The height of the tip and of the dot over the plane are 40 nm and 20 nm, respectively. The figure shows that the obtained signal is strongly enhanced under the edges of the tip indicating that the resolution is given by the diameter of the tip. Figure 11 presents the signal for a scan in y direction at $x=0\mu\text{m}$ for different parameters. In Fig. 11(a) different linewidths are considered, showing an approximately linear dependence of the coupling to the particular susceptibility. For a medium with gain $\chi_0=-1$ the observed signal shows a sign change in comparison to the absorbing case $\chi_0=1$.

Figure 11(b) compares different scanning heights (40 nm, 50 nm, 60 nm) implying different distances of tip and sample (20 nm over the surface). The results show that the dot induced signal strongly decreases relative to the surrounding interference pattern when the tip has a larger distance from

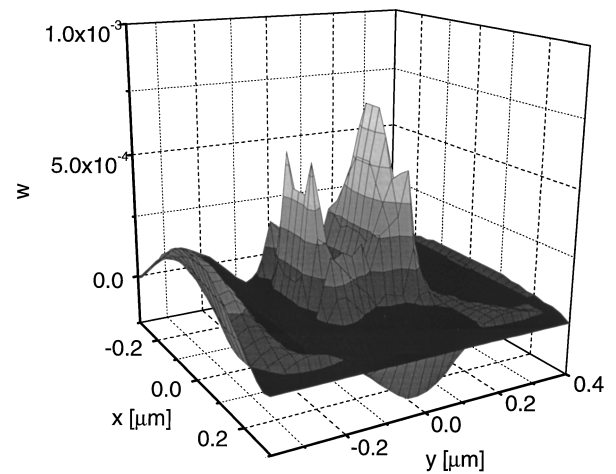


FIG. 10. Signal of one dot, detected in the collection mode, the dot with susceptibility $\chi_0=1$ is placed in $(0,0)$.

the surface. The oscillating variations of the signal are caused by the interference of the incoming wave and field scattered by the sample (negative y in Figs. 11) and the interference of the incoming wave and field scattered by the tip (positive y in Fig. 11). Only if these variations are small in comparison with the signal due to the direct interaction of tip and sample can the sample be analyzed in a useful way. This is the case if the distance between tip and dot is in the region of the diameter of the sample.

(ii) *Dot arrays.* Figure 12 shows a two dimensional scan over three dots at the positions $(-0.4, 0.4)\mu\text{m}$, $(0, 0.3)\mu\text{m}$, and $(0.3, 0.2)\mu\text{m}$. The signal is strongly influenced by interferences between incoming surface wave and waves scattered by the quantum dots. However at the density assumed the dots are easily resolved and each dot is characterized by

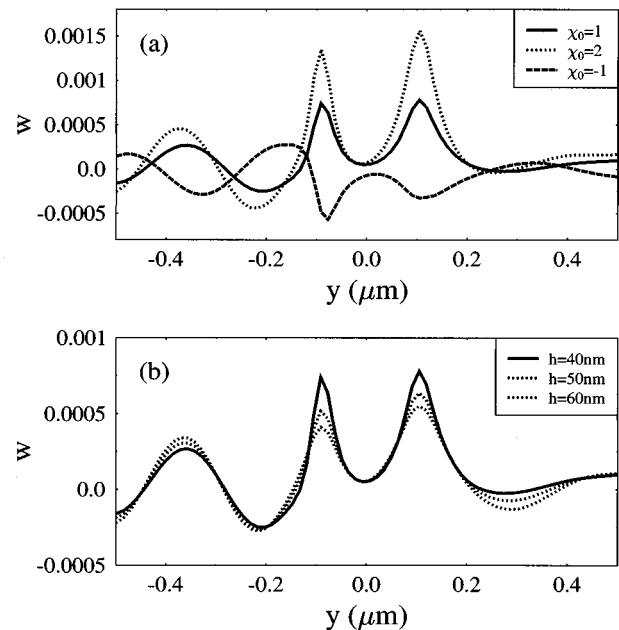


FIG. 11. Signal of one dot placed at $x, y=0$ in the collection mode for (a) different susceptibilities and (b) different scanning heights.

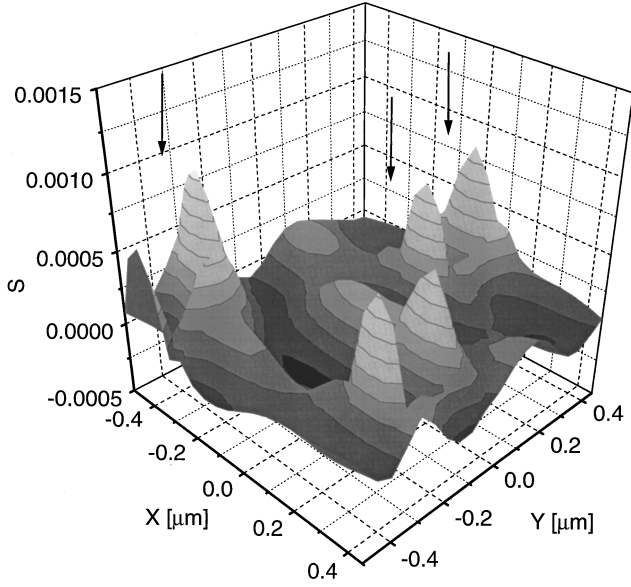


FIG. 12. Signal of three dots in collection mode. The dots are placed in $(-0.4, -0.4)\mu\text{m}$ and $(0.3, 0.3)\mu\text{m}$, and $(0.3, -0.2)\mu\text{m}$.

a double peak, which has approximately the size of the tip. The maxima of the peaks are twice as high as the maximum of the surrounding wiggles. However this contrast depends strongly on the dot density due to a competition effect between interfering fields which enhance the contrast for increasing dot density and the overlap of the main peaks under the tip walls [similar to Fig. 8(a)].

V. CONCLUSIONS

In conclusion, we have discussed the equations of motion for an array of quantum dots interacting with the near-field distribution of a fiber tip. Within these equations, a single quantum dot couples with the other quantum dots and the near-field tip via the self-consistent electric and magnetic field at the position of the dot. In contrast to the situation of far-field excitation where the magnetic field is often neglected, the magnetic field may be enhanced in comparison to the electric field if very small apertures are used. Hence, more interaction terms than the well known electric dipole coupling may be important in the material equations (compare with the appendix). However, for the tips used in these calculations, which come close to the tips used in recent experiments, the magnetic field enhancement turns out to be negligible. Thus, the numerical solutions presented here focus on the material coupling to the electric field.

The investigation of a single dot indicates that the near-field induces strong line shape changes only if the ratio of the intrinsic linewidth and the transition frequency is smaller than 10^{-9} . For extremely small ratios even a splitting of the line which results from the strong coupling between the tip and dot is observed. The field distributions in the collection and illumination mode show that the signal is strongly enhanced at the metallic edges of the tip. The investigation of an array of dots shows that as long as the dot density is as low as one per tip extension in the scanning direction the dots can be measured independently. In this case the emitted fields can be viewed as a linear superposition of individual

dots. The analysis is more complicated if the dot density is larger, especially if the dots have different oscillator strengths, which is the case, e.g., for dots with a size distribution. In this case interference effects prevent a unique interpretation of the obtained signal and a supporting calculation of the tip-dot interaction must be carried out.

We compare the two modes regarding the strength of the signal, which is the relative change of energy density or energetic flux induced by the presence of the dot. For a resonantly excited dot with $\chi_0=1$ the signal has a maximum of 0.0002 in the illumination mode and 0.0007 in the collection mode. For the collection mode, on the other hand, there are strong interference effects from the scattering of the surface wave by the dot. The variations of the signal due to this effect make the detection of the dot impossible, unless the distance of the tip and sample is very small. A numerical analysis indicates that the illumination mode is not limited by this. In both cases the resolution is of the order of the tip diameter. In general, it seems that the resolution could be improved by using imperfect metallized tips, where only one wall guides the field to the object. In this case, the resolution of the tip is of the order of the wall width.

ACKNOWLEDGMENTS

This work was supported by the Deutsche Forschungsgemeinschaft (Germany), partially through the SFB Contract No. 383. We acknowledge discussions with S. Grosse, J. Feldmann, and F. Jahnke who brought the Green function method of Ref. 9 to our attention, and K. Karrai.

APPENDIX A: GREEN FUNCTION METHOD

In this appendix we briefly review a recently published Green function method⁹ to solve the wave equation Eq. (6) for the electric field. The Green function $\hat{\mathbf{G}}$ (here a 3×3 tensor) for the electric field in the wave equation is defined by

$$\{\nabla^2 - \nabla \nabla \cdot + k^2[\varepsilon_r(\mathbf{r}) + \varepsilon_p(\mathbf{r})]\}\hat{\mathbf{G}}(\mathbf{r}, \mathbf{r}') = \hat{\boldsymbol{\delta}}(\mathbf{r} - \mathbf{r}'), \quad (\text{A1})$$

where the dyadic δ function is given by $\hat{\boldsymbol{\delta}}(\mathbf{r}) = \delta(\mathbf{r}) \sum \delta_{ij} \mathbf{e}_i \otimes \mathbf{e}_j$. In the following $\hat{\mathbf{G}}^r$ denotes the Green function for the reference system only, this means the solution of Eq. (A1) for $\varepsilon_p=0$. The division of ε into a reference system, described by ε_r and a perturbation ε_p is done in such a way that for the reference system the Green function $\hat{\mathbf{G}}^r$ is known, and also a solution of the homogeneous wave equation \mathbf{E}_0 , representing the incident field.

Let S be the region to which the perturbation is restricted, this means ε_p vanishes outside of S . The full Green function can then be calculated via the standard Dyson equation:

$$\hat{\mathbf{G}}(\mathbf{r}_1, \mathbf{r}_2) = \hat{\mathbf{G}}^r(\mathbf{r}_1, \mathbf{r}_2) \quad (\text{A2})$$

$$-k^2 \int_S \hat{\mathbf{G}}^r(\mathbf{r}_1, \mathbf{r}') \varepsilon_p(\mathbf{r}') \hat{\mathbf{G}}(\mathbf{r}', \mathbf{r}_2) d\mathbf{r}'.$$

With the help of $\hat{\mathbf{G}}$ electric fields within the perturbation

$$\mathbf{E}(\mathbf{r}) = \mathbf{E}_0(\mathbf{r}) - k^2 \int_S \hat{\mathbf{G}}(\mathbf{r}, \mathbf{r}') \varepsilon_p(\mathbf{r}') \mathbf{E}_0(\mathbf{r}') d\mathbf{r}' \quad (\text{A3})$$

as well as outside of S ,

$$\mathbf{E}(\mathbf{r}) = \mathbf{E}_0(\mathbf{r}) - k^2 \int_S \hat{\mathbf{G}}^r(\mathbf{r}, \mathbf{r}') \varepsilon_p(\mathbf{r}') \mathbf{E}(\mathbf{r}') d\mathbf{r}', \quad (\text{A4})$$

can be calculated. The computational problem is to solve the Dyson equation (A2) for $\hat{\mathbf{G}}(\mathbf{r}, \mathbf{r}')$ with \mathbf{r}, \mathbf{r}' in the source region S . An effective scheme to solve the Dyson equation has been proposed in Ref. 9. The key idea is the following feature inherent to the structure of the Dyson equation: If the perturbation ε_p is split into two parts $\varepsilon_p = \varepsilon_p^1 + \varepsilon_p^2$, the Dyson Eq. (A2) can be solved for $\varepsilon_p = \varepsilon_p^1$, defining the Green function $\hat{\mathbf{G}}^1$ of the perturbation ε_p^1 alone. $\hat{\mathbf{G}}^1$ can be regarded as a new reference system, thus inserting $\hat{\mathbf{G}}^1$ for $\hat{\mathbf{G}}^r$ and ε_p^2 for ε_p into Dyson equation (A2) now defines the total $\hat{\mathbf{G}}$. This is an alternative way for solving Eq. (A2) in two steps instead of one. This procedure works not only for splitting into two parts but for splitting into arbitrary n .

All involved functions are discretized in real space $f_i = f(\mathbf{r}_i)$ into n components, and the perturbation ε_p is split into n parts ε_p^l , $l=1, n$ where the components are chosen to be $\varepsilon_{pi}^l = \varepsilon_p(\mathbf{r}_i) \delta_{il}$, $i=1, n$. In this case the summation in the Dyson equation vanishes and the following n equations have to be solved:

$$\hat{\mathbf{G}}_{ij}^l = \hat{\mathbf{G}}_{ij}^{l-1} - k^2 \hat{\mathbf{G}}_{il}^{l-1} \varepsilon_i V_l \hat{\mathbf{G}}_{lj}^l, \quad (\text{A5})$$

starting from $l=1$ to $l=n$, with $\hat{\mathbf{G}}^0 = \hat{\mathbf{G}}^r$ and $\hat{\mathbf{G}}^m = \hat{\mathbf{G}}$. V_l denotes the volume of the site l . Each Eq. (A5) is solved for $j=l$ first (this is only a 3×3 linear equation system), inserting $\hat{\mathbf{G}}_{il}^l$ again leaves us with $\hat{\mathbf{G}}_{ij}^l$ for arbitrary i, j .

This method does not require that the value ε_p is small, however, for each step the whole field $\hat{\mathbf{G}}_{ij}^l$ is required. Numerically this is mainly a storage problem, e.g., a mesh of 500 points with 16 byte per complex number leaves us with about 35 MB. So the region S of the source has to be bounded and the scheme is most effective for a localized perturbation.

APPENDIX B: MATERIAL EQUATIONS

In this appendix, the material equations for electromagnetic near-field excitation of a quantum dot are derived and a comparison of the results with far-field excitation is given. The Hamiltonian for a system of charge carriers in external potentials \mathbf{A}, U read:

$$H = \frac{1}{2m} \sum_i \left(\mathbf{p}_i + \frac{e}{c} \mathbf{A}(\mathbf{r}_i, t) \right)^2 - \sum_i eU(\mathbf{r}_i, t) + H_{\text{int}}, \quad (\text{B1})$$

where the Hamiltonian H_{int} contains the internal electromagnetic interaction of the electrons with charge e and their interaction with the ion background. Because the carriers are well localized in a quantum dot, one can take advantage of a Poincaré-gauge transformation for the external potentials (see Ref. 15). The Poincaré gauge requires the new potentials to have the form:

$$\mathbf{A}' = - \int_0^1 d\mathbf{u} \mathbf{r} \times \mathbf{B}(\mathbf{u} \mathbf{r}), \quad U' = - \int_0^1 d\mathbf{u} \mathbf{r} \cdot \mathbf{E}(\mathbf{u} \mathbf{r}).$$

After a multipole expansion the Hamiltonian for a single quantum dot at $R=0$ reads

$$H = H_0 - \mathbf{d} \cdot \mathbf{E}(0, t) - \mathbf{m} \cdot \mathbf{B}(0, t), \quad (\text{B2})$$

where $\mathbf{d} = -e \sum_i \mathbf{r}_i$ is the electric dipole moment and $\mathbf{m} = -(e/c) \sum_i \mathbf{r}_i \times \mathbf{p}_i$ is the magnetic dipole moment of the dot. The Hamiltonian H_0 contains the internal electromagnetic interaction of the particles as well as their kinetic energy. Note, that the occurring \mathbf{E} field is the total electric field which contains longitudinal and transverse components. To proceed, the formalism of the second quantization is applied for the material dipole moments which are expanded in the eigenfunctions of the Hamiltonian H_0 :

$$H = \sum_i E_i a_i^\dagger a_i - \sum_{ij} \mathbf{d}_{ij} \mathbf{E}(t) a_i^\dagger a_j - \sum_{ij} \mathbf{m}_{ij} \mathbf{B}(t) a_i^\dagger a_j. \quad (\text{B3})$$

Here, a_i^\dagger, a_i are the construction and destruction operators for a electron within the quantum state i which is supposed to be an eigenstate of the Hamiltonian H_0 .

At this point it is worth while to discuss an important difference between far-field and near-field optics. For far-field excitation the multipole expansion is usually truncated after the electric dipole term, thus neglecting the magnetic term, with the following argument. For transverse fields (far fields) one has $|\mathbf{E}| \approx |\mathbf{B}|$, and the related interaction energies in the Hamiltonian can be estimated to be different by the fine structure constant α , modified by semiconductor material parameters, $\mathbf{d}_{ij} \cdot \mathbf{E} / \mathbf{m}_{ij} \cdot \mathbf{B} \approx \alpha \ll 1$. In the case of an optical near field, the estimation of the different parts in the Hamiltonian is more difficult because the electrical and the magnetic fields are not necessarily on the same order of magnitude. However, a rough estimate is possible if the Bethe-Bouwkamp solution⁷ is used to estimate the fields in a small circular aperture. The magnetic fields are enhanced by a factor $(ak)^{-1}$, $|\mathbf{E}|/|\mathbf{B}| \approx ak$, with a being the aperture radius and $k = \omega/c$ the wave number of the incident light. For realistic apertures this may be of the order of $1-100$. Thus, electric and magnetic terms in the Hamiltonian (B2) may be of the same order of magnitude. These estimations are only valid in the case of $ak \ll 1$, and it is questionable to generalize them for tips used in today's experiments. Therefore, we did calculations of the magnetic field. They indicate that the magnetic terms can indeed be neglected (see section on the characterization of the tip, Fig. 5). As indicated by these numerical calculations, the used apertures are still too large to make the magnetic field important. Thus only the electric dipole interaction will be considered in the following.

In the strong quantization limit (small dots) where we neglect the formation of excitons and biexcitons, the quantum number i contains the conduction or valence band number $\mu = c, v$, as well as the subband number n of the envelope function in a confinement potential: $|i\rangle = \xi_{n_i} \mu_{\mu_i}$. In this case, the dipole moments are given by the following integrals over the volume of the dot:

$$\mathbf{d}_{\mu_1\mu_2}^{n_1n_2} = -e \int_{\Omega_0} dV u_{\mu_1}^* \mathbf{r} u_{\mu_2} \delta_{n_1, n_2} - e \int_{\text{dot}} dV \xi_{n_1}^*(\mathbf{R}) \mathbf{R} \xi_{n_2}(\mathbf{R}) \delta_{\mu_1, \mu_2}. \quad (\text{B4})$$

Here, Ω_0 is one elementary cell. As can be recognized, the electric field induces intersubband transitions within the valence and the conduction band. In this paper, we focus on the lowest subband in the quantum confined potential only and restrict the calculations to a two band model with a strict s -like conduction band and a p -like valence band, hence

$n_i = c, v$ only. To derive the susceptibility which enters in the wave equation as a source, the equation for the polarization \mathbf{P} has to be derived:

$$\mathbf{P} = \sum_{\mu_1, \mu_2} a_{\mu_1}^\dagger a_{\mu_2} d_{\mu_1, \mu_2}. \quad (\text{B5})$$

Calculating the Heisenberg equations of motion and taking the expectation value of the polarization, the standard expression for the susceptibility Eq. (8) is obtained. The generalization for many quantum dots at different positions is straightforward.

-
- ¹L. Banyai and S. W. Koch, *Semiconductor Quantum Dots*, World Series On Atomic, Molecular and Optical Physics Vol. 2, (World Scientific, Singapore, 1993).
- ²U. Woggon, *Optical Properties of Semiconductor Quantum Dots*, Springer Tracts in Modern Physics Vol. 136 (Springer, Berlin, 1996).
- ³A. Zrenner, L. V. Butov, M. Hagn, G. Abstreiter, G. Böhm, and G. Weimann, Phys. Rev. Lett. **72**, 3382 (1994).
- ⁴D. Gammon, E. S. Snow, B. V. Shanabrook, D. S. Katzer, and D. Park, Phys. Rev. Lett. **76**, 3005 (1996).
- ⁵D. W. Pohl, in Adv. Opt. Electron Microsc. **12**, 248 (1991).
- ⁶H. A. Bethe, Phys. Rev. **66**, 163 (1944).
- ⁷C. J. Bouwkamp, Philips Res. Rep. **5**, 401 (1950).
- ⁸L. Novotny, D. W. Pohl, and B. Hecht, Opt. Lett. **20**, 970 (1995).
- ⁹O. J. F. Martin, C. Girard, and A. Dereux, Phys. Rev. Lett. **74**, 526 (1995).
- ¹⁰C. Girard, O. J. F. Martin, and A. Dereux, Phys. Rev. Lett. **75**, 3098 (1995).
- ¹¹R. X. Bian, R. C. Dunn, X. S. Xie, and P. T. Leung, Phys. Rev. Lett. **75**, 4772 (1995).
- ¹²M. J. Gregor, P. G. Blome, R. G. Ulbrich, P. Grossmann, S. Grosse, J. Feldmann, W. Stolz, E. O. Göbel, D. J. Arent, M. Bode, K. A. Bertness, and J. M. Olson, Appl. Phys. Lett. **67**, 3572 (1995).
- ¹³J. D. Jackson, *Classical Electrodynamics* (Wiley, New York, 1962).
- ¹⁴W. W. Rühle, A. Kurtenbach, and K. Eberl, Il Nuovo Cimento **17**, 1305 (1995).
- ¹⁵C. Cohen-Tannoudji, *Photons and Atoms* (Wiley, New York, 1989).